Supplementary Material

This document supplements data and discussions on DEM simulation conditions, DEM granular temperature, numerical methods for FDM simulations, effects of μ_2 and μ_3 in inclined chute flows, limitations of the first-order model, and the fluctuation energy balance.

S1 DEM SIMULATION CONDITIONS

Table S1. Simulation conditions for the planar shear tests (3D spheres with $\mu_p = 0.4$)

Geometry	N	P_{wall}/P_0	G/G_0	V_{wall}/V_0	Δn	N_{out}
Simple shear	18327	4		0.003125	160000	7200
Simple shear	18327	4		0.0125	80000	3600
Simple shear	18327	4		0.05	40000	3600
Simple shear	18327	1		0.1	40000	3600
Simple shear	18327	1		0.2	40000	3600
Simple shear	18327	1		0.4	40000	3600
Simple shear	18327	1		0.8	10000	7200
Simple shear	18327	1		1.6	10000	7200
Simple shear	18327	1		3.2	10000	7200
Simple shear	18327	1		6.4	5000	14400
Simple shear	6923	1		6.4	40000	3600
Shear with gravity	18327	1	16	3.2	20000	7200
Shear with gravity	18327	1	2	12.8	20000	7200
Shear with gravity	18327	1	32	1.6	40000	3600
Shear with gravity	18327	1	4	6.4	40000	7200
Shear with gravity	18327	1	8	1.6	40000	3600
Shear with gravity	18327	4	8	0.1	40000	3600
Shear with gravity*	18327	1	16	3.2	40000	7200
Shear with gravity*	18327	1	2	12.8	5000	14400
Shear with gravity*	18327	1	32	1.6	40000	7200
Shear with gravity*	18327	1	4	6.4	40000	7200
Chute flows ($\theta = 90°$)	18327	8.8	12		40000	14400
Chute flows ($\theta = 90°$)	18327	8.8	16		40000	14400
Chute flows ($\theta = 90°$)	18327	8.8	20		40000	14400
Chute flows ($\theta = 60°$)	18327	8.8	16		40000	3600
Chute flows ($\theta = 60°$)	18327	8.8	20		40000	3600
Chute flows ($\theta = 60°$)	18327	8.8	24		40000	3600
Chute flows ($\theta = 60°$)	18327	8.0	16		40000	14400
Chute flows ($\theta = 60°$)	18327	8.0	20		40000	14400
Concave flows	18327	16	3.5	0.00625	80000	7200
Concave flows	18327	16	3	0.025	40000	14400
Concave flows	18327	16	3	0.4	40000	14400
Concave flows	18327	16	3	1.6	20000	14400

* Shear with gravity using a fixed steady-state wall height

Table S1 shows detailed simulation conditions for the planar shear tests. N is the total number of particles except wall particles. The wall pressure P_{wall} and gravity G are given by material constants k_n, d, and ρ_s. We use $k_n = 2.63 \times 10^5$N/m, $d = 0.0008$m, and $\rho_s = 2500\text{Kg}/\text{m}^3$. In the table, the unit of pressure P_0 and acceleration G_0 are $3.1 \times 10^{-7} k_n/d$ and $(1/50)P_0/\rho_s d$ respectively. The unit of velocity V_0 is $8.8\sqrt{P_0/\rho_s}$. We output data every Δn steps to take a total of N_{out} snapshots.

Table S2. Simulation conditions for the inclined chute flows (3D spheres with $\mu_p = 0.4$)

Geometry	N	G/G_0	$\tan\theta$	Δn	N_{out}
Inclined chute flows	115619	64	0.47	40000	7200
Inclined chute flows	115619	64	0.50	40000	7200
Inclined chute flows	115619	64	0.55	40000	7200
Inclined chute flows	115619	64	0.60	40000	7200

Table S2 shows simulation conditions for the inclined chute flows. θ is the angle of inclination. The other constants are the same as those of the planar shear tests.

S2 DEM GRANULAR TEMPERATURE

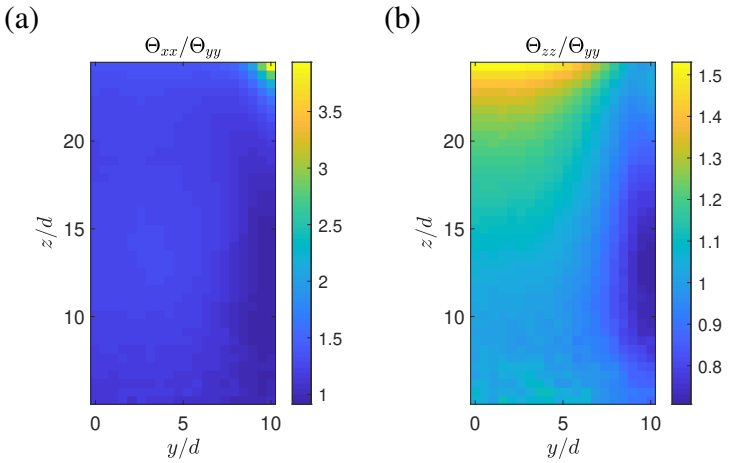

Figure S1. Ratios between diagonal elements of the granular temperature tensor from the DEM simulation of the inclined chute flow with $\tan\theta = 0.60$: (a) Θ_{xx}/Θ_{yy} and (b) Θ_{zz}/Θ_{yy}. The maximum value of Θ_{xx}/Θ_{yy} is approximately 4 at the upper right corner, while Θ_{zz}/Θ_{yy} distributes between 0.7 and 1.5.

When we extract Θ from the DEM data, we exclude Θ_{xx} because it is measured curiously large at some parts of the flows. Figure S1 visualizes the ratios between diagonal elements of the granular temperature tensor. Most noticeably, Θ_{xx} is measured up to four times larger than Θ_{yy} at the upper corner of the system in the fastest flow with $\tan\theta = 0.60$ as shown in Figure S1a. Such a large difference has not been observed in the planar shear flows. This may be because, near the boundary between the two systems, the particles moving in the opposite directions collide each other and their relative velocities are, on average, larger in the x-direction. On the other hand, Θ_{yy} and Θ_{zz} are quite similar. Θ_{zz}/Θ_{yy} distributes only between 0.7 and 1.5 as shown in Figure S1b. We therefore choose to exclude Θ_{xx} that behaves uniquely and use $(\Theta_{yy} + \Theta_{zz})/2$ as Θ. The granular temperature anisotropy and its impact on the constitutive equations should be further studied in the future.

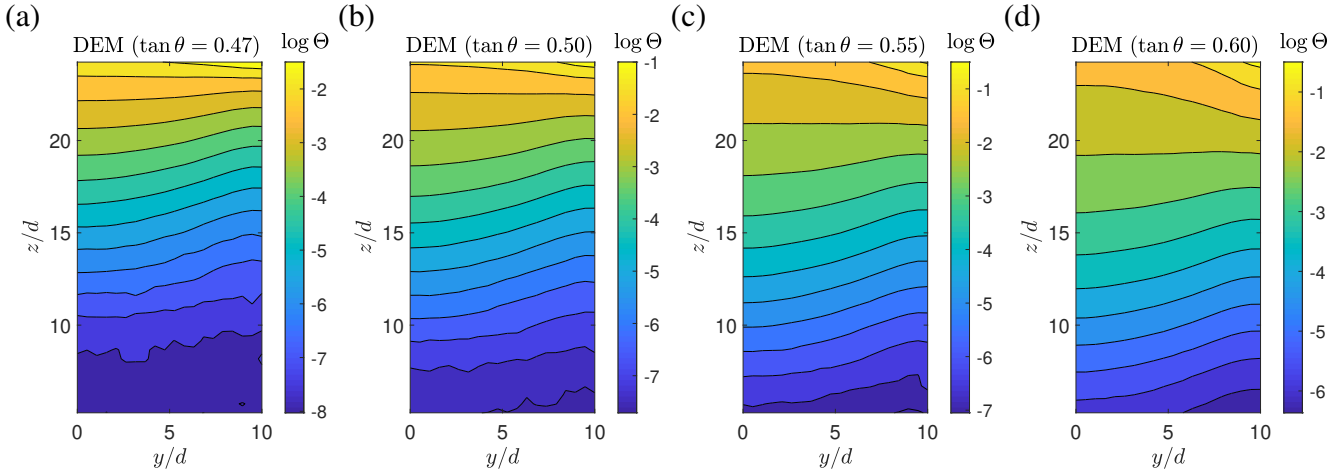

Figure S2. Contours of $\log\Theta \equiv \log\left[(\Theta_{yy} + \Theta_{zz})/2\right]$ from the DEM simulations of the inclined chute flow with (a) $\tan\theta = 0.47$, (b) $\tan\theta = 0.50$, (c) $\tan\theta = 0.55$, and (d) $\tan\theta = 0.60$. These data are used to calculate $\mu_1(I, \Theta)$ and $\mu_2(I, \Theta)$ in the FDM simulations.

Figure S2 plots contours of $\log\Theta$ which is defined as $\log\left[(\Theta_{yy}+\Theta_{zz})/2\right]$ obtained from the DEM simulations with four different inclination angles. Almost equally separated contours except near the surface indicate that Θ decays exponentially with depth. It is interesting that near the surface Θ is higher at the side boundary ($y = 10d$), but below a certain height Θ is higher at the center of the flow ($y = 0$). That is because the inertial number that affects the velocity fluctuations behaves in a similar way. It is hard for the material to have $\partial_y v_x$ at the frictional bottom, and it is also hard to have $\partial_z v_x$ at $y = 10d$ due to the symmetry of the geometry. Therefore, at the bottom corner ($y = 10d, z = z_{\text{min}}$), the shear rate should be very small while the material can still have $\partial_z v_x$ at the bottom center. It results in the downward convex Θ contours below a certain height. Near the top, on the other hand, Θ is larger at $y = 10d$ because the material is far from the bottom such that it can have a large $|\partial_y v_x|$ and the pressure is smaller at $y = 10d$ than $y = 0$ due to the bulging surface. These data are used to compute μ_1 and μ_2 in the second-order model.

S3 NUMERICAL METHODS FOR FDM SIMULATIONS

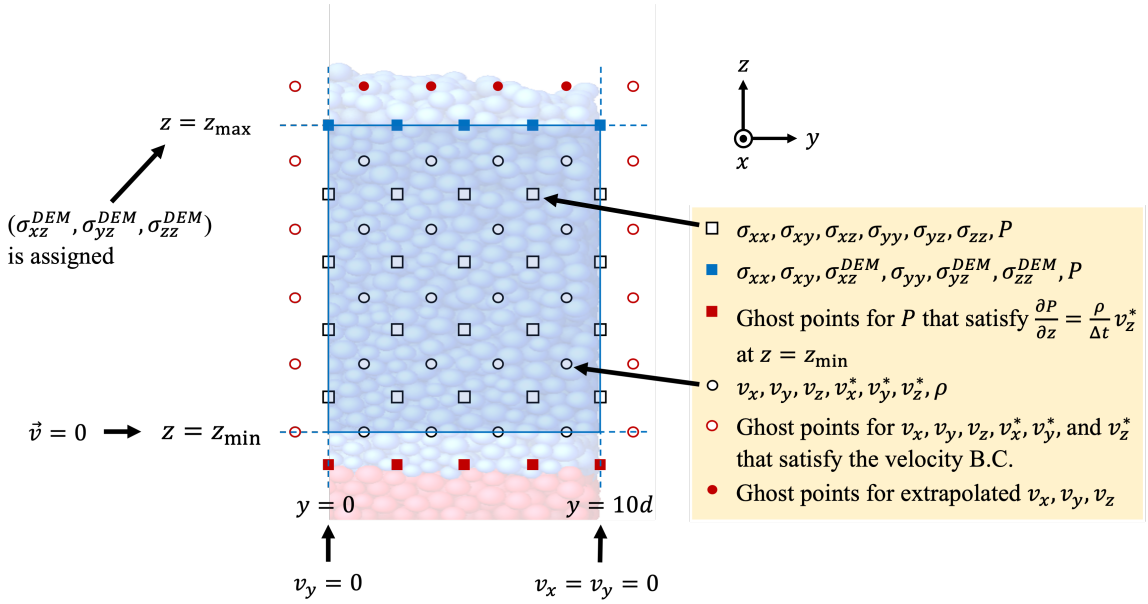

Figure S3. Schematic diagram of the FDM simulation grid. Squares represent stress points while circles represent velocity points. Sky blue box indicates physical domain where stress and velocity are computed ($z_{\min} = 5.49d$ and $z_{\min} = 24.25d$). Red points outside the physical domain are ghost points to set boundary conditions.

Figure S3 illustrates the finite difference method (FDM) simulation grid, which is the half-staggered grid where the velocity grid points are located at the center points of the stress grid cells. The stress grid points are marked as squares and the velocity grid points are marked as circles.

For the first derivatives except for $(\boldsymbol{v}^n \cdot \nabla)\boldsymbol{v}^n$, variables at four points around the point of interest are used to obtain their central difference. For $(\boldsymbol{v}^n \cdot \nabla)\boldsymbol{v}^n$, we use the first-order upwind scheme in which the upstream variable and the variable at the point of interest are used to calculate the first derivative [1] even though the effect of this term is very small.

To obtain the pressure, we numerically solve Eq. (24). The discrete Poisson equation for the five pressure values around the point (i, j) (i is the index in the y-direction and j is the index in the z-direction) can be written as

$$\alpha(P_{i+1,j} + P_{i-1,j}) + \beta(P_{i,j+1} + P_{i,j-1}) - 2(\alpha + \beta)P_{i,j} = f_{ij} \tag{S1}$$

where $\alpha = (\Delta y)^{-2}$, $\beta = (\Delta z)^{-2}$, and f_{ij} is the discrete value of $\frac{1}{\Delta t}\nabla \cdot (\rho \boldsymbol{v}^*)$ at the point (i, j) obtained from the surrounding four $\rho \boldsymbol{v}^*$ values. Due to the system symmetry, the pressure values at the ghost nodes Δy outside the side boundaries are naturally set to be the pressure values at the physical nodes Δy inside the boundaries. The pressure values at the bottom ghost nodes are given such that $\frac{\partial P}{\partial z} = \frac{\rho}{\Delta t} v_z^*$ at $z = z_{\min}$ is satisfied assuming zero physical velocity at the bottom. The pressure at $z = z_{\max}$ is given by dividing the DEM σ_{zz} by the σ_{zz} to P ratio expected from the velocity gradient at $z = z_{\max}$. To calculate this velocity gradient, we exploit ghost velocity values at $z = z_{\max} + \Delta z$ using the extrapolation from the previous FDM velocity below $z_{\max}$.

Then the set of Poisson equations for all the nodes can be simply represented as a matrix equation

$$\boldsymbol{L}\boldsymbol{p} = \boldsymbol{f} - \beta\boldsymbol{q} \tag{S2}$$

where

$$\boldsymbol{L} = \begin{bmatrix} \boldsymbol{A}+\boldsymbol{B} & \boldsymbol{B} & \boldsymbol{O} & \dots & \dots & \dots & \boldsymbol{O} \\ \boldsymbol{B} & \boldsymbol{A} & \boldsymbol{B} & \boldsymbol{O} & \dots & \dots & \boldsymbol{O} \\ \boldsymbol{O} & \boldsymbol{B} & \boldsymbol{A} & \boldsymbol{B} & \boldsymbol{O} & \dots & \boldsymbol{O} \\ \vdots & \ddots & \ddots & \ddots & \ddots & \ddots & \vdots \\ \boldsymbol{O} & \dots & \boldsymbol{O} & \boldsymbol{B} & \boldsymbol{A} & \boldsymbol{B} & \boldsymbol{O} \\ \boldsymbol{O} & \dots & \dots & \boldsymbol{O} & \boldsymbol{B} & \boldsymbol{A} & \boldsymbol{B} \\ \boldsymbol{O} & \dots & \dots & \dots & \boldsymbol{O} & \boldsymbol{B} & \boldsymbol{A} \end{bmatrix} \tag{S3}$$

is the $mn \times mn$ Laplace operator with the given boundary conditions,

$$\boldsymbol{A} = \begin{bmatrix} -2(\alpha+\beta) & 2\alpha & 0 & \dots & \dots & \dots & 0 \\ \alpha & -2(\alpha+\beta) & \alpha & 0 & \dots & \dots & 0 \\ 0 & \alpha & -2(\alpha+\beta) & \alpha & 0 & \dots & 0 \\ \vdots & \ddots & \ddots & \ddots & \ddots & \ddots & \vdots \\ 0 & \dots & 0 & \alpha & -2(\alpha+\beta) & \alpha & 0 \\ 0 & \dots & \dots & 0 & \alpha & -2(\alpha+\beta) & \alpha \\ 0 & \dots & \dots & \dots & 0 & 2\alpha & -2(\alpha+\beta) \end{bmatrix} \tag{S4}$$

and $\boldsymbol{B} = \beta\boldsymbol{I}$. $\boldsymbol{A}$ and $\boldsymbol{B}$ are both $m \times m$. $\boldsymbol{p}$ is a column vector composed of the pressure values:

$$\boldsymbol{p} = [P_{11}, P_{21}, ..., P_{m1}, P_{12}, P_{22}, ..., P_{m2}, ..., P_{mn}]^T \tag{S5}$$

$\boldsymbol{f}$ is a column vector composed of $f_{ij} = \frac{1}{\Delta t}\left[\nabla \cdot (\rho \boldsymbol{v}^*)\right]_{ij}$. $\boldsymbol{q}$ is another column vector given by $\boldsymbol{q} = \left[\Delta \boldsymbol{p}_{z_{\min}}^T, 0, \dots, 0, \boldsymbol{p}_{z_{\max}}^T\right]^T$ determining the top and bottom boundary conditions. $\Delta\boldsymbol{p}$ is the column vector of pressure difference between the two bottom rows set by $-\Delta z \left(\frac{\partial P}{\partial z}\right)_{z_{\min}} = -\Delta z \left(\frac{\rho}{\Delta t} v_z^*\right)_{z_{\min}}$ and $\boldsymbol{p}_{z_{\max}}$ is the pressure at the top row obtained from the DEM σ_{zz} and the extrapolated velocity gradient at $z = z_{\max}$. The size of $\boldsymbol{p}$ is $mn \times 1$, and $\Delta\boldsymbol{p}_{z_{\min}}$ and $\boldsymbol{p}_{z_{\max}}$ are $m \times 1$. Using MATLAB, we can numerically solve the system of linear equations Eq. (S2) to obtain the solution $\boldsymbol{p}$.

S4 EFFECTS OF μ_2 AND μ_3 IN INCLINED CHUTE FLOWS

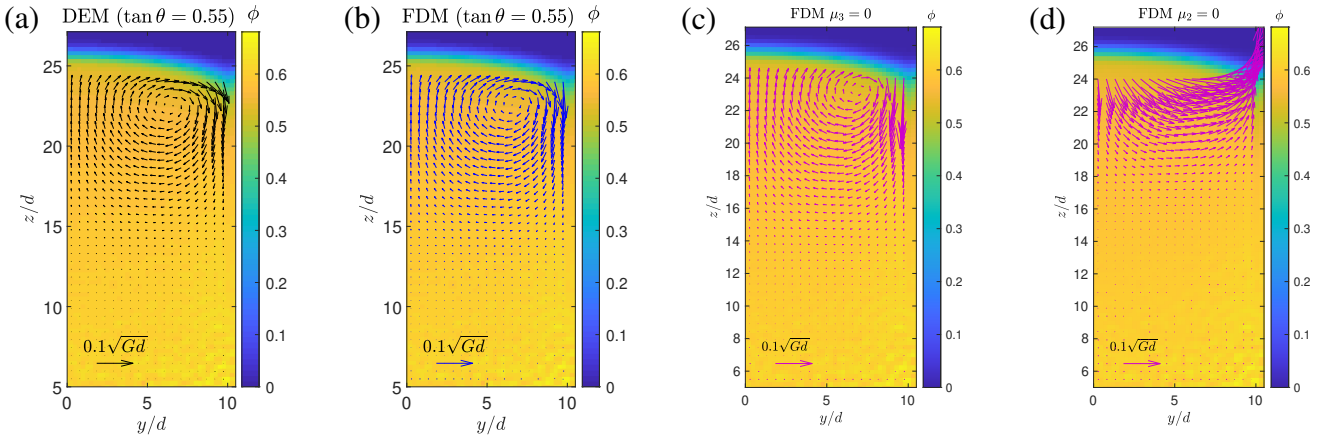

Figure S4. Comparison of the effects of μ_2 and μ_3 in the inclined chute flows: Transverse velocity fields for $\tan\theta = 0.55$ predicted by (a) DEM data, (b) the full second-order model, (c) the second-order model with $\mu_3 = 0$, and (d) the second-order model with $\mu_2 = 0$. The traction at the upper boundary is given by the DEM simulation. Arrows indicate (v_y, v_z) and their length scales are displayed at the bottom of the figures. Packing fraction is shown as color in the background. Comparing (c) and (d), we can see that μ_2 is more important in describing the transverse flow.

If we keep μ_3 and set μ_2 to zero, the prediction of the transverse flow becomes totally different from the DEM data as can be seen in Figure S4d. However, if we keep μ_2 and set μ_3 to zero, the FDM simulation still generates similar secondary flows (Figure S4c) even though the results are not as accurate as the full second-order model's (Figure S4b).

S5 LIMITATIONS OF THE FIRST-ORDER MODEL

Let us prove that the first-order model cannot predict the transverse velocity components for a free surface flow (no surface traction) by assuming the steady-state solution has no transverse components: $\boldsymbol{v} = (u(y,z),0,0)$. Then the velocity gradient tensor only has two nonzero elements, $\partial_y u$ and $\partial_z u$, which results in $\sigma_{xx} = \sigma_{yy} = \sigma_{zz} = -P$, $\sigma_{yz} = 0$, $\sigma_{xy} = \mu P(\partial_y u)/\dot{\gamma}$ and $\sigma_{xz} = \mu P(\partial_z u)/\dot{\gamma}$ where $\dot{\gamma} = \sqrt{(\partial_y u)^2 + (\partial_z u)^2}$. Using this stress tensor, the momentum balance can be expressed as $\partial_z \sigma_{zz} - \rho G_z = 0$ where $G_z = G\cos\theta$ in the z-direction and $\partial_y \sigma_{yy} = 0$ in the y-direction. These two equations give a simple linear lithostatic pressure $P(z)$. The momentum balance in the x-direction reads $\partial_y \sigma_{xy} + \partial_z \sigma_{xz} + \rho G_x = 0$ where $G_x = G\sin\theta$. This gives a partial differential equation for $u(y,z)$ with the surface boundary condition $\partial_z u = 0$ as $\sigma_{xz} = 0$. As in Kim and Kamrin [2], $u(y,z)$ can be solved from this PDE and the boundary conditions. This system must have a unique nontrivial solution, and we have proven that the solution has a form of $\boldsymbol{v} = (u(y,z),0,0)$. Also, the fact that the system with traction-free upper boundary has a steady state solution with zero transverse velocities implies that the surface would stay flat if the fluid follows the first-order model. It means the first-order model cannot explain the convex surface in the DEM simulations.

If an external surface traction from DEM is applied, the first-order model can have nonzero v_y and v_z. In this case, σ_{yz} is no longer zero and transverse velocities are generated to match this stress. However, we have checked with the first-order models that their FDM solutions to the transverse velocities are completely different from the DEM data as can be seen in Figure S5

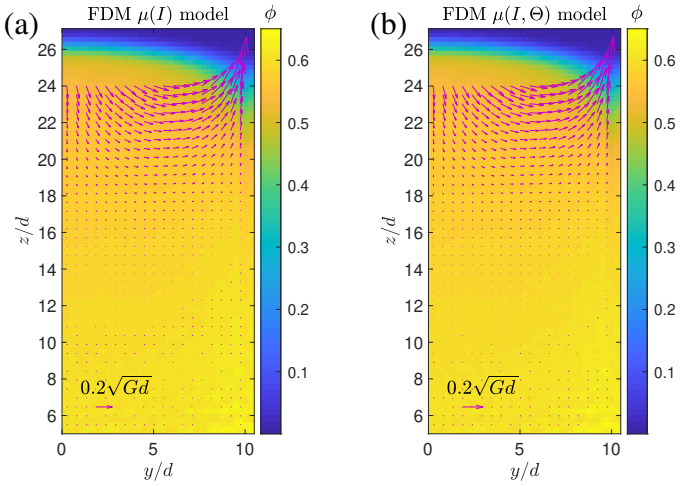

Figure S5. Transverse velocity fields for $\tan\theta = 0.60$ predicted by (a) the $\mu(I)$ model and (b) the $\mu(I,\Theta)$ model when the traction at the upper boundary is given by the DEM simulation. Arrows indicate (v_y, v_z) and their length scales are displayed at the bottom of the figures. Packing fraction is shown as color in the background. The transverse velocities are not zero due to the input traction, but very different from the DEM velocity field in Figure 11D.

S6 FLUCTUATION ENERGY BALANCE

The granular temperature is governed by the fluctuation energy balance which has long been an interest in the kinetic theory [3, 4, 5]. The most general form is given by

$$\frac{3}{2}\rho\frac{DT}{Dt} = -\nabla\cdot\vec{q} + \tau\dot{\gamma} - \Gamma \tag{S6}$$

where $\vec{q} = -\kappa\nabla T$ is the flux of fluctuation energy, $\tau\dot{\gamma}$ is the self-heating rate (the rate of work done by shear stress), and Γ is the rate of energy dissipation due to inelastic collision and frictional sliding. Eq. (S6) is very similar to the differential equation in the NGF model which, when taken to the stable and steady-state only limit, has the diverging length scale. This length could be seen as stemming from the length-scale in κ. Also, Zhang and Kamrin [6] found g is locally approximated with a multiplication of $\sqrt{T}$ and a function of packing fraction. These similarities suggest that the NGF model may be a nice approximation of the fluctuation energy balance [7]. The kinetic theory has expressed κ and Γ in terms of T and ϕ, but it has hardly been verified empirically in the dense limit. To predict the granular temperature, future studies should identify this differential equation more accurately.

REFERENCES

[1] Courant R, Isaacson E, Rees M. On the solution of nonlinear hyperbolic differential equations by finite differences. *Communications on Pure and Applied Mathematics* **5** (1952) 243–255. doi:https://doi.org/10.1002/cpa.3160050303.

[2] Kim S, Kamrin K. Power-law scaling in granular rheology across flow geometries. *Physical Review Letters* **125** (2020) 088002. doi:10.1103/PhysRevLett.125.088002.

[3] Jenkins JT, Savage SB. A theory for the rapid flow of identical, smooth, nearly elastic, spherical particles. *Journal of Fluid Mechanics* **130** (1983) 187–202. doi:10.1017/S0022112083001044.

[4] Lun CKK, Savage SB, Jeffrey DJ, Chepurniy N. Kinetic theories for granular flow: inelastic particles in couette flow and slightly inelastic particles in a general flowfield. *Journal of Fluid Mechanics* **140** (1984) 223–256. doi:10.1017/S0022112084000586.

[5] Bocquet L, Losert W, Schalk D, Lubensky TC, Gollub JP. Granular shear flow dynamics and forces: Experiment and continuum theory. *Physical Review E* **65** (2001) 011307. doi:10.1103/PhysRevE.65.011307.

[6] Zhang Q, Kamrin K. Microscopic description of the granular fluidity field in nonlocal flow modeling. *Physical Review Letters* **118** (2017) 058001. doi:10.1103/PhysRevLett.118.058001.

[7] Kamrin K. Non-locality in granular flow: Phenomenology and modeling approaches. *Frontiers in Physics* **7** (2019). doi:10.3389/fphy.2019.00116.